# Bright Infrared Emission from Electrically Induced Excitons in Carbon Nanotubes

Jia Chen,[1*] Vasili Perebeinos,[1] Marcus Freitag,[1] James Tsang,[1] Qiang Fu,[2] Jie Liu,[2] Phaedon Avouris[1*]

We used the high local electric fields at the junction between the suspended and supported parts of a single carbon nanotube molecule to produce unusually bright infrared emission under unipolar operation. Carriers were accelerated by band-bending at the suspension interface, and they created excitons that radiatively recombined. This excitation mechanism is ~1000 times more efficient than recombination of independently injected electrons and holes, and it results from weak electron-phonon scattering and strong electron-hole binding caused by one-dimensional confinement. The ensuing high excitation density allows us to observe emission from higher excited states not seen by photoexcitation. The excitation mechanism of these states was analyzed.

The optical properties of single-walled semiconducting carbon nanotubes (CNTs) are currently the focus of intense study (*1–8*). CNTs are direct band-gap materials, and their optical spectra have long been attributed to transitions between free-particle bands. Theoretical studies, on the other hand, have pointed out that there should be strong electron-hole ($e^-$-$h^+$) interactions in these quasi–one-dimensional (1D) materials, resulting in strongly bound excitons (*9–11*). Recent experimental evidence for the formation of CNT excitons is provided by two-photon fluorescence excitation spectroscopy (*3*) and photoconductivity (*8*). CNTs offer the possibility of a unified electronic and optoelectronic technology (*12*). Therefore, it is important to understand electroluminescence (EL) from CNTs. Moreover, the study of EL provides further insights into $e^-$-$h^+$ interactions in quasi-1D materials.

Here we discuss an excitation mechanism that leads to a strongly enhanced EL in the infrared (IR) from a partially suspended CNT field-effect transistor (CNTFET) operating under unipolar transport conditions. In light-emitting diodes (LEDs) or ambipolar CNTFETs, the participating carriers (both $e^-$ and $h^+$) are injected from the source and drain electrodes separately (*2*, *13*). In our devices, carriers are generated locally when a single type of carrier is accelerated under high local electric field to energies sufficient to create strongly correlated $e^-$-$h^+$ pairs (excitons).

This impact excitation process differs greatly in 3D and 1D systems. In bulk 3D semiconductors, the weak Coulomb interaction between $e^-$ and $h^+$ creates weakly bound excitons (*14*) that mostly dissociate under high field and contribute to the electrical current (*15*). In 1D CNTs, on the other hand, exciton binding energies are predicted to be more than an order of magnitude larger (*9–11*), so that the 1D excitons are expected to recombine and contribute little to the current. We find that the intensity of light emission increases exponentially with the drive current in partially suspended CNTFETs [in 3D materials, light emission is usually proportional to the product of the $e^-$ and $h^+$ currents (*14*)] and has a similar dependence on both the gate and drain bias, whereas the current itself increases linearly with bias.

These observations are a manifestation of the strong $e^-$-$h^+$ interactions in the quasi-1D CNTs that prevent $e^-$-$h^+$ pairs from dissociating and validate the exciton picture. We also find that the current-voltage (*I-V*) characteristics of the suspended CNTFETs display negative differential conductance (NDC), which, by comparison with the light emission, we find to be correlated with the onset of the generation of excitons by hot carriers (*16*). This local EL mechanism leads to a $10^2$ to $10^3$ times increase in efficiency over that achieved by supported ambipolar CNTFETs (*16*). From both the position of the emission spot and the dependence of the IR emission on the drain and gate bias, we conclude that the high local electrical field at the suspension interface is mainly responsible for the enhanced emission efficiency. By removing the underlying substrate and suspending the CNT, nonradiative recombination channels involving the substrate can also be reduced (*5*). The extraordinary current-carrying capability of a CNT (*12*) and its ultra-small size lead to an ultra-bright light source. Finally, the ~100 times higher exciton density (0.14 $nm^{-1}$) achieved in our devices, compared with that in typical photoluminescence (PL) experiments, allows us to detect emission from the second allowed exciton ($E_{22}$) state in CNTs. We show that $E_{11}$ exciton-exciton annihilation is primarily responsible for the $E_{22}$ emission. In agreement with a very recent study (*17*), where high exciton densities were achieved in PL using pulsed laser excitation, we did not see direct evidence for a Mott transition, which is expected to take place when excitons start to spatially overlap.

The CNTFETs (~25 devices) with a partially suspended CNT channel used in this study were fabricated by etching 0.4-to-15-μm-wide trenches in a 200-nm-thick $SiO_2$ film on Si wafers. The trenches extended through the $SiO_2$ film and 2 μm into the Si substrate. CNTs with diameters in the range of 2 to 3 nm were grown on the trenched substrate by chemical vapor deposition (*18*). Palladium source and drain electrodes were then patterned on CNTs with channel lengths between 4 and 80 μm. The highly doped silicon substrate was used as a back gate. Detailed experimental setup and sample fabrication are discussed in the supporting online materials (*18*).

A spatial map of the IR emission, collected with a bandpass filter centered around 1.6 μm (in the $E_{11}$ emission band) from a single CNTFET, was superimposed on an optical image of the device structure (Fig. 1A). Unlike nonsuspended CNTFETs, whose emission from ambipolar injection can be spatially translated along the length of a CNT by changing the gate bias (*13*), the emission from the partially suspended device is localized at the $SiO_2$ supported/suspended CNT interfaces under a wide range of gate biases. Figure 1B shows the drain current and the emission intensity at 1.6 μm occurring at the suspension interface, as a function of the gate voltage ($V_g$) at a constant drain bias of $V_d = -5$ V. We observed no detectable emission when the gate bias was below a threshold gate overdrive $|V_g - V_{th}|$ of ~0.5 V, where $V_{th}$ is the threshold voltage (–2.6 V in this sample) at which the CNTFET is electrically turned on. At $|V_g - V_{th}| > 0.5$ V, the emission intensity increases rapidly with increasing current.

There are three major differences in the IR emission from suspended CNTFETs compared with that from nonsuspended devices: (i) The dominant emission from the suspended CNT occurs under unipolar transport conditions ($V_g < -3.1$ V for $h^+$ and $V_g > -2.1$ V for $e^-$), and no appreciable emission is observed at the ambipolar region where the current shows a minimum ($V_g = -2.6$ V); (ii) The emission intensity increases exponentially with the drive current in the suspended tube (Fig. 1B, inset), whereas in a nonsuspended CNT biased under ambipolar conduction, the emission intensity is proportional to the minority carrier density (*19*); (iii) The minimum drain bias needed to observe emission is notably smaller in sus-

[1]IBM Research Division, Thomas J. Watson Research Center, Post Office Box 218, Yorktown Heights, NY 10598, USA. [2]Department of Chemistry, Duke University, Durham, NC 27708, USA.

*To whom correspondence should be addressed. E-mail: chenjia@us.ibm.com (J.C.); avouris@us.ibm.com (P.A.)

pended tubes ($V_d \sim 2.5$ V) than that in nonsuspended tubes ($V_d \sim 15$ V) (*13*). In turn, a CNTFET operated under ambipolar conditions needs to be driven to higher drain/gate fields and currents to generate the same amount of light as the suspended CNT, indicating that EL via ambipolar conduction is a much less efficient process. Indeed, the emission efficiency defined as photons per electron measured on the suspended samples (*16*) is about $10^{-3}$ to $10^{-4}$, that is, the partially suspended samples exhibit an increase of 2 to 3 orders of magnitude from that of supported CNTs operated under ambipolar conduction conditions (*16*). Although the efficiency (photons/electron) of the suspended CNTs is numerically comparable to that of CNTs wrapped in micelles in PL measurements (emitted photons/adsorbed photon) (*1*), the small optical cross section of CNTs ($10^{-11}$ to $10^{-12}$ cm$^2$ per CNT) (*20*) reduces the effectiveness of exciton generation by photoexcitation. For a typical injection current of 3 μA, ~20 electrons per ps are injected in a steady state in a CNT, generating ~0.02 photons per ps by EL; correspondingly, $\sim 2 \times 10^{13}$ cm$^{-2}$ ps$^{-1}$ per CNT input photons are required by photoexcitation. The small emitting area coupled with the high current-density–carrying capability in a CNT makes it possible to produce an ultra-bright nano–light emitter. For example, a 3-μA current in a partially suspended CNTFET generates about $10^7$ photons nm$^{-2}$ s$^{-1}$.

How is the light generated in the supported/suspended CNT interface? Figure 1C shows a schematic band diagram of a partially suspended CNT with a gate biased to produce unipolar conduction. At the junction between the $SiO_2$-supported part of the CNT and the part suspended over the trench, the decrease in dielectric constant (*21*) leads to a reduced capacitive coupling to the Si back gate. This process gives rise to a bending of the CNT bands, which, together with the source-drain field, generates a high local electric field $\mathcal{E}$ and produces hot carriers. Thus, electrons injected into the conduction band are accelerated toward the source by the high field at the interface. If an electron can be accelerated to a sufficiently high energy and does not lose that energy by optical phonon scattering, it can create an exciton that can decay radiatively. The electron that lost energy to the generated exciton could, in turn, pick up energy from the field and continue this process. For an impact excitation process to occur, both energy and momentum need to be conserved. The threshold energy should be at least equal to the lowest exciton energy, and the need to conserve momentum typically increases the threshold energy by a factor of ~1.5 (*22*). Exciton-band–mixing effects (*10*, *11*) and interactions with the substrate can, however, relax the momentum conservation law, and the threshold energy can be as low as the exciton energy.

A rough estimate of the threshold electrical field $\mathcal{E}_{th}$ needed for impact excitation is given by $1.5E_g/\lambda_{ph}$, where $E_g$ is the transition energy [optical band gap ~ 0.56 eV for a 1.9-nm-diameter CNT (*23*)] and $\lambda_{ph} \approx 10$ to 20 nm is the optical phonon scattering length reported in CNTs (*24*, *25*). Compared with 3D materials (*22*), the longer optical phonon scattering length implies a lower threshold field for the onset of impact excitation in 1D CNTs, whereas the larger exciton binding energy in 1D CNTs prevents e$^-$-h$^+$ pairs from dissociating. These two factors make emission from impact excitation in 1D a more probable process than that in 3D materials. Indeed, $\mathcal{E}_{th}$ for the 1D CNT is estimated to be $\sim 1.5E_g/\lambda_{ph} = 0.3$ to 0.6 MV/cm, i.e., it is ~7 times smaller than that in bulk materials with the same excitation energy (*22*).

The emission intensity generated by the high interface field $\mathcal{E}_{int}$ should be proportional to the impact excitation rate (*22*), $\exp(-\mathcal{E}_{th}/\mathcal{E}_{int})$. The probability for an electron to travel without scattering a distance $L$ is given by $\exp(-L/\lambda_{ph})$. Therefore, the probability to accelerate an electron to energy $E_{th}$ is $\exp(-E_{th}/e\mathcal{E}_{int}\lambda_{ph})$, where $e$ is the electron charge and where field $\mathcal{E}_{int}$ has contributions from both the band-bending and the source-drain fields, $\mathcal{E}_{band}$ and $\mathcal{E}_{sd}$, respectively. $\mathcal{E}_{band}$ can be estimated as $\Delta E_c/\lambda_{scr} \sim [\alpha_{sub}(V_g - V_{th}) - \alpha_{sus}(V_g - V_{th})]/\lambda_{scr}$ (*26*), where $\Delta E_c$ is the band bending, $\alpha_{sub}$ is the coupling between the gate and the substrate-supported CNT, $\alpha_{sus}$ is the coupling between the gate and the suspended CNT, and $\lambda_{scr}$ is the screening length (*27*). $\mathcal{E}_{sd}$ is the contribution from the source-drain field that accelerates the carriers, and can be written as $\sim\gamma V_d/\lambda_{scr}$, where γ is the fraction of the source-drain field that contributes to the $SiO_2$ supported/suspended interface junction. The IR emission intensity of the radiatively recombining e$^-$-h$^+$ pairs is proportional to the carrier impact excitation rate

$$\exp(-\mathcal{E}_{th}/\{[(\alpha_{sub} - \alpha_{sus}) \times (V_g - V_{th}) + \gamma V_d]/\lambda_{scr}\}) \quad (1)$$

We first examine the dependence of emission intensity on the gate bias. Figure 2A shows the drain current of another suspended device and the corresponding IR emission intensity at 1.6 μm (within the $E_{11}$ emission band) versus gate voltage $V_g$ at drain biases of $V_d = 6$ and 7 V. IR emission occurs at a gate voltage overdrive of ~2 V. The IR emission is localized at the supported/suspended interface (Fig. 2A, inset). The emission intensity indeed shows the dependence on the gate field predicted by Eq. 1 and can be fit for both drain biases, as shown by the solid curves in Fig. 2A. From the fitting, a γ of 0.05 is obtained at both drain biases. A band-bending of ~0.4 eV at the peak of light emission can be estimated from electrostatics (*27*). $\mathcal{E}_{int}$ in our device is estimated to be 0.01 to 0.2 MV/cm for the fields at the onset and the peak of light emission.

We now turn to the dependence of light emission on the source-drain field. Figure 2B shows the drain current $I_d$ and light emission at 1.6 μm versus drain bias $V_d$ at constant gate biases of $V_g = 0$ and 1 V of the same device. Unlike CNTs on solid substrates (*13*), the following is true for suspended devices: (i) Approximately 6 times lower drain bias is sufficient under unipolar conduction to generate light emission, benefiting from the high local field generated by the band-bending at the suspended/supported CNT interface. (ii) The suspended devices show NDC in their $I_d - V_d$ characteristics. The appearance of NDC correlates with the observation of IR emission (Fig. 2B). At its onset, impact excitation is expected to generate nonemitting triplet excitons followed, at higher energy, by light-emitting singlet excitons (*28*). The observed NDC could be

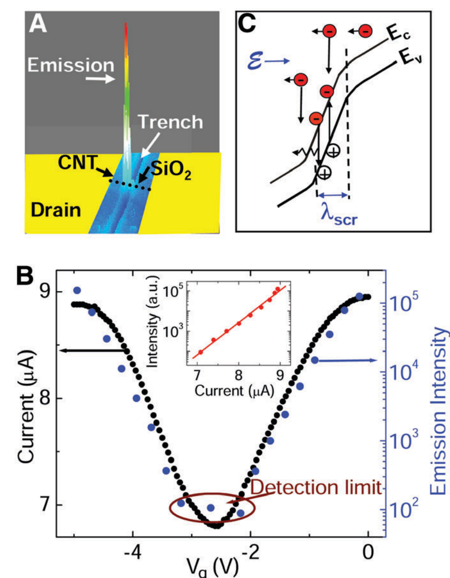


**Fig. 1.** (**A**) $E_{11}$ infrared emission overlaid with an optical image of a partially suspended CNTFET with 200 nm $SiO_2$, Pd source/drain contacts and a Si back gate. The length of the channel is 26 μm, the width of the trench is 5 μm, and the CNT diameter is ~2 nm. (**B**) Drain current (solid squares) and emission intensity (solid circles) versus gate bias at 1.6 μm of a partially suspended CNTFET at $V_d = -5$ V. One unit of emission intensity corresponds to about 240 photons per second per 4π solid angle in all the following figures. The inset shows the emission intensity increases exponentially with drive current. The solid line is meant as a guide to the eyes. (**C**) Schematics of impact excitation process. An incoming hot electron is accelerated by the band-bending at the suspended/supported interface to energies larger than the band gap and generates an exciton that decays radiatively. Subsequently, the "cooled" electron picks up more energy from the electrical field and continues this process.

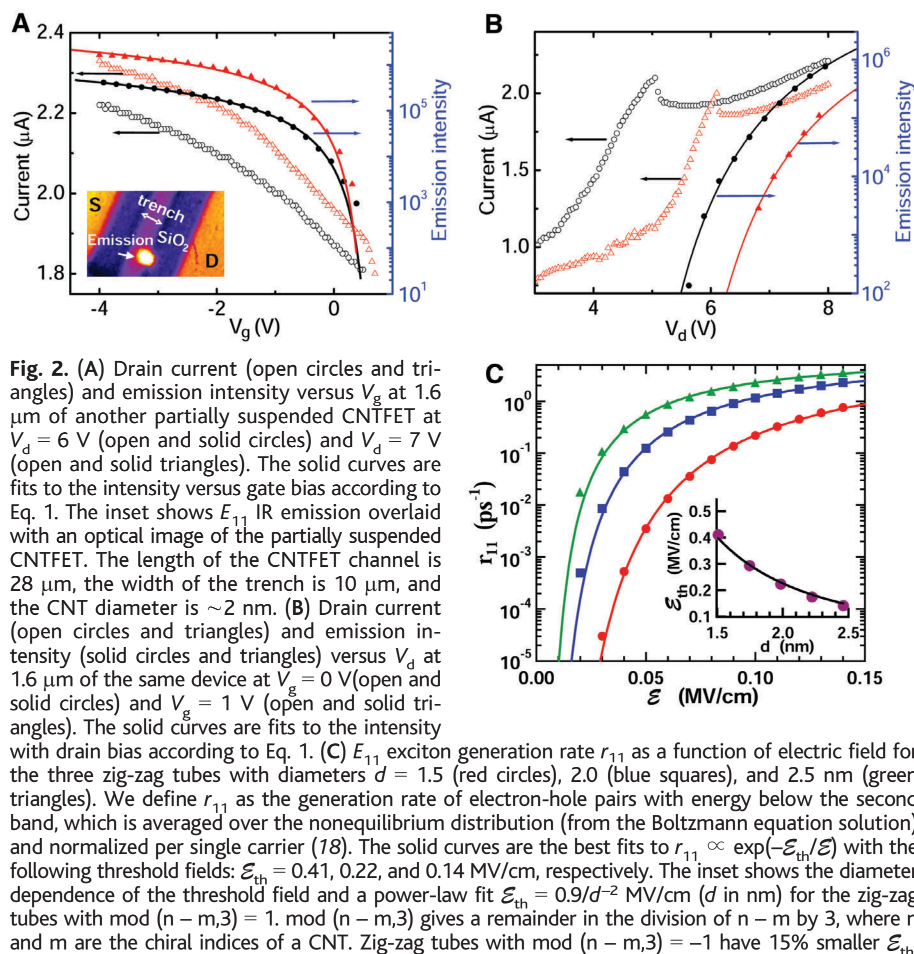


**Fig. 2.** (**A**) Drain current (open circles and triangles) and emission intensity versus $V_g$ at 1.6 μm of another partially suspended CNTFET at $V_d$ = 6 V (open and solid circles) and $V_d$ = 7 V (open and solid triangles). The solid curves are fits to the intensity versus gate bias according to Eq. 1. The inset shows $E_{11}$ IR emission overlaid with an optical image of the partially suspended CNTFET. The length of the CNTFET channel is 28 μm, the width of the trench is 10 μm, and the CNT diameter is ~2 nm. (**B**) Drain current (open circles and triangles) and emission intensity (solid circles and triangles) versus $V_d$ at 1.6 μm of the same device at $V_g$ = 0 V(open and solid circles) and $V_g$ = 1 V (open and solid triangles). The solid curves are fits to the intensity with drain bias according to Eq. 1. (**C**) $E_{11}$ exciton generation rate $r_{11}$ as a function of electric field for the three zig-zag tubes with diameters $d$ = 1.5 (red circles), 2.0 (blue squares), and 2.5 nm (green triangles). We define $r_{11}$ as the generation rate of electron-hole pairs with energy below the second band, which is averaged over the nonequilibrium distribution (from the Boltzmann equation solution) and normalized per single carrier (*18*). The solid curves are the best fits to $r_{11} \propto \exp(-\mathcal{E}_{th}/\mathcal{E})$ with the following threshold fields: $\mathcal{E}_{th}$ = 0.41, 0.22, and 0.14 MV/cm, respectively. The inset shows the diameter dependence of the threshold field and a power-law fit $\mathcal{E}_{th} = 0.9/d^{-2}$ MV/cm ($d$ in nm) for the zig-zag tubes with mod (n – m,3) = 1. mod (n – m,3) gives a remainder in the division of n – m by 3, where n and m are the chiral indices of a CNT. Zig-zag tubes with mod (n – m,3) = –1 have 15% smaller $\mathcal{E}_{th}$.

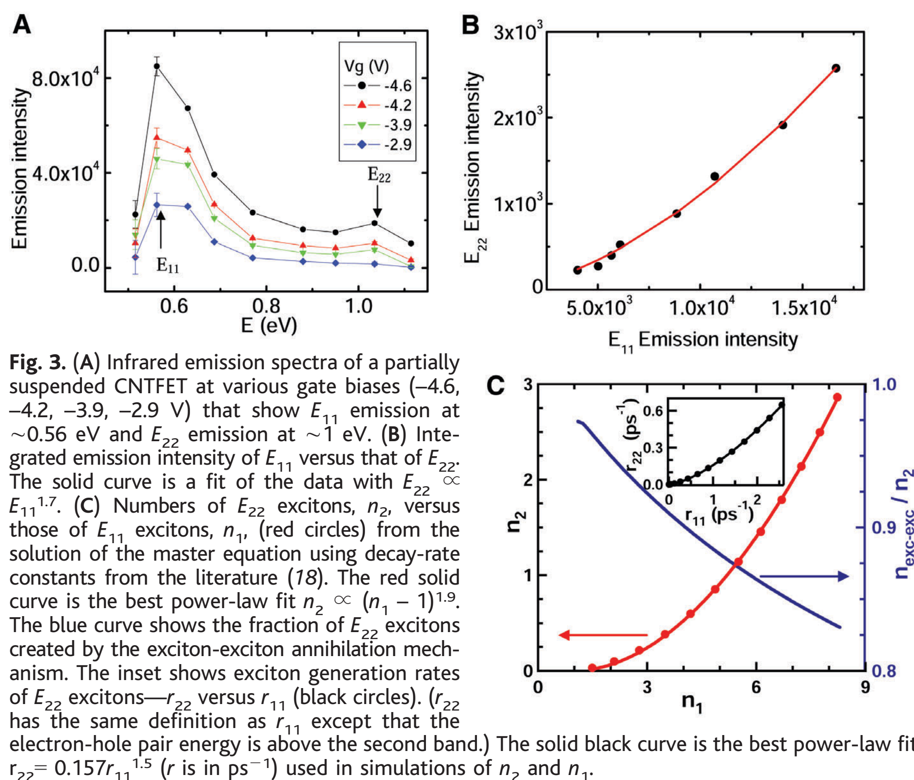


**Fig. 3.** (**A**) Infrared emission spectra of a partially suspended CNTFET at various gate biases (–4.6, –4.2, –3.9, –2.9 V) that show $E_{11}$ emission at ~0.56 eV and $E_{22}$ emission at ~1 eV. (**B**) Integrated emission intensity of $E_{11}$ versus that of $E_{22}$. The solid curve is a fit of the data with $E_{22} \propto E_{11}^{1.7}$. (**C**) Numbers of $E_{22}$ excitons, $n_2$, versus those of $E_{11}$ excitons, $n_1$, (red circles) from the solution of the master equation using decay-rate constants from the literature (*18*). The red solid curve is the best power-law fit $n_2 \propto (n_1 - 1)^{1.9}$. The blue curve shows the fraction of $E_{22}$ excitons created by the exciton-exciton annihilation mechanism. The inset shows exciton generation rates of $E_{22}$ excitons—$r_{22}$ versus $r_{11}$ (black circles). ($r_{22}$ has the same definition as $r_{11}$ except that the electron-hole pair energy is above the second band.) The solid black curve is the best power-law fit $r_{22} = 0.157 r_{11}^{1.5}$ ($r$ is in ps$^{-1}$) used in simulations of $n_2$ and $n_1$.

attributed to the momentum loss from impact excitation of excitons. In a gate scan where gate overdrive $|V_g - V_{th}|$ is a variable (Fig. 1C and Fig. 2A), the momentum loss from the charged carriers that have undergone impact excitation can be compensated by the increase in the carrier density caused by the increasing gate overdrive. Therefore, no further reduction of current is observed. The light-emission intensity shows a dependence on the drain field that is also in accord with Eq. 1 and can be fit for both gate biases as shown by the solid curves in Fig. 2B. By biasing the device at different gate overdrives with $|V_g - V_{th}| \approx 2$ and 1 V for $V_g$ = 0 and 1 V, respectively, we find that indeed a higher drain field is necessary ($\Delta V_d = +1$ V) to compensate a lower gate overdrive ($\Delta|V_g - V_{th}| \approx -1$ V) in order for impact excitation to take place.

To understand the voltage dependences of the light-emission intensity, we calculated the exciton generation rate as a function of the electric field by solving the Boltzmann equation in the presence of phonon and impact excitation scattering for the charge-carrier distribution function (*18*). The results of the calculations are shown in Fig. 2C for three CNTs with different diameters along with the best fit to $I \propto \exp(-\mathcal{E}_{th}/\mathcal{E})$ predicted by the simple model. In agreement with experiment, impact excitation does not take place for fields below 0.02 to 0.03 MV/cm. The diameter dependence of the threshold field can be well approximated by a power law $\mathcal{E}_{th} \propto E_g/\lambda_{ph} \propto d^{-2}$ (Fig. 2C, inset), as a result of both the inversely proportional dependence between $E_g$ and the CNT diameter $d$ and the proportional dependence between $\lambda_{ph}$ and $d$. We calculate $\lambda_{ph}$ here as the ratio of the impact excitation threshold energy to the threshold field and find it in the range of 20 to 40 nm (for $d$ =1.5 to 2.5 nm CNTs), in accord with previous studies (*24*, *25*, *29*).

The high local density of excitons produced at the suspended/supported CNT interface allows us to directly observe exciton-exciton interactions. Studies of the dynamics of excitation decay in photoexcited CNTs in micelles have shown a nonexponential, laser power–dependent decay, whose short time component was attributed to Auger quenching involving free carriers (*3*, *30*) or exciton-annihilation processes (*31*, *32*). In addition to the exciton-exciton interaction, direct generation of $E_{22}$ excitons by hot carriers is possible in EL. By examining the evolution of the EL spectrum as a function of the gate voltage and from the results of our simulations, we conclude that $E_{11}$ exciton-exciton annihilation is primarily responsible for the production of $E_{22}$ excitons. Figure 3A shows the spectra of a partially suspended, 1.9-nm-diameter tube at various gate biases and a fixed $V_d$ of –5 V. The strong emission peak at 0.56 eV corresponds very well with the lowest optically active transition of the CNT, $E_{11}$, observed in PL experiments (*23*).

In the EL experiments, however, a weaker peak near 1 eV is also observed. The energy of the transition lies at the expected position of the second optically allowed transition, $E_{22}$, of the CNT [with $E_{11}/E_{22}$ ~1.8, also consistent with that of PL studies (*23*)]. The nature of the excitation mechanism of this state is revealed by examining the light emission intensity of $E_{22}$ as a function of the intensity of $E_{11}$ and the results of our simulations (*18*). Figure 3B shows that $I(E_{22}) \propto I(E_{11})^{1.7}$. This nonlinear dependence alone cannot distinguish between a direct exciton-generation mechanism and a "bimolecular" exciton-exciton annihilation [$E_{11} + E_{11} \rightarrow E_{22}$ (+ phonons)] process. Indeed, the direct impact excitation rate of $E_{22}$ also has a power-law dependence on $E_{11}$ generation (Fig. 3C, inset). Further carrier-kinetics calculations using the master equation (*18*) indicate that the formation of $E_{22}$ excitons is primarily caused by the annihilation of two $E_{11}$ excitons. There is a negligible $E_{22}$ exciton density until the exciton-exciton annihilation process becomes possible (Fig. 3C), which is consistent with the experimental data in Fig. 3A. The fraction of $E_{22}$ excitons generated by the exciton-exciton annihilation mechanism gradually decreases with increasing field, from 100% to slightly above 80% for the typical fields achieved in our devices. From the master equation (*18*), we estimate that there are about eight $E_{11}$ excitons at the intrananotube junction at a field of 0.15 MV/cm. The total exciton density (0.14 $nm^{-1}$) is therefore about 100 times larger than what has been reported in typical PL experiments (*32*), making it possible to observe the "bimolecular" process. Such annihilation processes are widely observed in molecular crystals, polymers, and j-molecular aggregates (*33*), and apparently play a key role in the photo- and electroluminescence of CNTs.

### References and Notes


1. S. M. Bachilo *et al.*, *Science* **298**, 2361 (2002).
2. J. A. Misewich *et al.*, *Science* **300**, 783 (2003).
3. F. Wang, G. Dukovic, L. E. Brus, T. F. Heinz, *Science* **308**, 838 (2005).
4. A. Hagen, G. Moos, V. Talalaev, T. Hertel, *Appl. Phys. A* **78**, 1137 (2004).
5. J. Lefebvre, Y. Homma, P. Finnie, *Phys. Rev. Lett.* **90**, 217401 (2003).
6. H. Htoon, M. J. O'Connell, S. K. Doorn, V. I. Klimov, *Phys. Rev. Lett.* **94**, 127403 (2005).
7. S. G. Chou *et al.*, *Phys. Rev. Lett.* **94**, 127402 (2005).
8. X. Qiu *et al.*, *Nano Lett.* **5**, 749 (2005).
9. T. Ando, *J. Phys. Soc. Jpn.* **66**, 1066 (1997).
10. C. D. Spataru, S. Ismail-Beigi, L. X. Benedict, S. G. Louie, *Phys. Rev. Lett.* **92**, 077402 (2004).
11. V. Perebeinos, J. Tersoff, P. Avouris, *Phys. Rev. Lett.* **92**, 257402 (2004).
12. P. Avouris, *Mater. Res. Soc. Bull.* **29**, 403 (2004).
13. M. Freitag *et al.*, *Phys. Rev. Lett.* **93**, 076803 (2004).
14. P. Y. Yu, M. Cardona, *Fundamentals of Semiconductors* (Springer, New York, 1996).
15. C. Tedesco *et al.*, *IEEE Trans Elec. Dev* **40**, 1211 (1993).
16. M. Freitag *et al.*, *Nano Lett.* **4**, 1063 (2004).
17. G. N. Ostojic *et al.*, *Phys. Rev. Lett.* **94**, 97401 (2005).
18. Details of sample fabrication, experimental methods, and simulations are available as supporting material on *Science* Online.
19. S. Heinze, J. Tersoff, P. Avouris, in *Introducing Molecular Electronics*, G. Cuniberti, G. Fagas, K. Richter, Eds. (Springer, New York, 2005), in press.
20. M. F. Islam, D. E. Milkie, C. L. Kane, A. G. Yodh, J. M. Kikkawa, *Phys. Rev. Lett.* **93**, 37404 (2004).
21. Trapped charge in silicon dioxide film could also contribute to CNT band-bending.
22. Y. Okuto, C. R. Crowell, *Phys. Rev. B* **6**, 3076 (1972).
23. B. Weisman, S. Bachilo, *Nano Lett.* **3**, 1235 (2003).
24. A. Javey *et al.*, *Phys. Rev. Lett.* **92**, 106804 (2004).
25. J. Y. Park *et al.*, *Nano Lett.* **4**, 517 (2004).
26. The band offset at the suspension/substrate interface, $\Delta E_c$, can be estimated from its coupling to the gate as $[\alpha_{sub}(V_g - V_{th}) - \alpha_{sus}(V_g - V_{th})]$, where $\alpha$ is the coupling between the gate bias and the band energy and can be estimated as $C_{el}/(C_{el} + C_q)$. Here $C_{el}$ is the electrostatic Si back gate–coupling capacitance, and $C_{el} = 2\pi\varepsilon\varepsilon_0 / \ln(4t/d)$, where $\varepsilon$ is the dielectric constant, $\varepsilon_0$ is the vacuum permittivity, $d$ is the CNT diameter, and $t$ is the thickness of the gate dielectric. For a CNT with $d$ = 1.9 nm on a 200-nm-thick $SiO_2$ ($\varepsilon$ = 3.9), $C_{el,substrate}/L \sim 0.36$ pF/cm; when the CNT is suspended 2 μm away from the gate, $C_{el,suspended}/L \sim 0.07$ pF/cm. $C_q$ is the quantum capacitance that is in series with the electrostatic capacitance (*34*), proportional to the average density of states [DOS, $D(E)$] of the nanotube, $C_q = dQ/dE \approx e^2D(E) \approx 4e^2/\hbar\pi v_F = 4$ pF/cm, where $Q$ is the charge on a CNT, $\hbar$ is the reduced Planck's constant, and $v_F$ is the Fermi velocity of graphene. This DOS is much larger than the electrostatic capacitance. In our device, $\alpha_{sub} \sim 0.09$ and $\alpha_{sus} \sim 0.02$.
27. $\lambda_{scr}$ can be roughly estimated as $(\varepsilon_{cnt}d_{cnt}d_{ox}/\varepsilon_{ox})^{0.5}$ for the transistor geometry (*35*), where ox indicates oxide, and its value is on the order of 20 to 40 $d_{cnt}$ in our devices. $\varepsilon_{cnt}$ can be estimated from (*36*).
28. V. Perebeinos, J. Tersoff, P. Avouris, *Nano Lett.*, in press.
29. V. Perebeinos, J. Tersoff, P. Avouris, *Phys. Rev. Lett.* **94**, 086802 (2005).
30. F. Wang, G. Dukovic, L. E. Brus, T. F. Heinz, *Phys. Rev. Lett.* **92**, 177401 (2004).
31. J. Kono *et al.*, *Appl. Phys. A* **78**, 1093 (2004).
32. Y. Ma, L. Valkunas, S. L. Dexheimer, S. M. Bachilo, G. R. Fleming, *Phys. Rev. Lett.* **94**, 157402 (2005).
33. H. van Amerongen, L. Valkunas, R. van Grondelle, *Photosynthetic Excitons* (World Scientific, Singapore, 2000).
34. A. Rahman, J. Guo, S. Datta, M. S. Lundstrom, *IEEE Trans. Electron Dev.* **50**, 1853 (2003).
35. R. H. Yan, A. Ourmazd, K. F. Lee, *IEEE Trans Electron Dev.* **39**, 1704 (1992).
36. L. X. Benedict, X. G. Louie, M. L. Cohen, *Phys. Rev. B* **52**, 8541 (1995).


37. We thank J. Rosner and Central Scientific Services for help with the optical mask design, and B. Ek for expert technical assistance.


**Supporting Online Material**
www.sciencemag.org/cgi/content/full/310/5751/1171/DC1
Materials and Methods
References


22 August 2005; accepted 24 October 2005
10.1126/science.1119177


# Retention of Xenon in Quartz and Earth's Missing Xenon


**Chrystèle Sanloup,[1]* Burkhard C. Schmidt,[2]† Eva Maria Chamorro Perez,[3] Albert Jambon,[1] Eugene Gregoryanz,[4] Mohamed Mezouar[5]**



**The reactivity of xenon with terrestrial oxides was investigated by in situ synchrotron x-ray diffraction. At high temperature ($T$ > 500 kelvin), some silicon was reduced, and the pressure stability of quartz was expanded, attesting to the substitution of some xenon for silicon. When the quartz was quenched, xenon diffused out and only a few weight percent remained trapped in samples. These results show that xenon can be covalently bonded to oxygen in quartz in the lower continental crust, providing an answer to the missing xenon problem; synthesis paths of rare gas compounds are also opened.**


The atmospheres of Earth and Mars are depleted in Xe by a factor of 20 relative to other rare gases (i.e., Ne, Ar, and Kr) (*1*). More than 99% of Xe was degassed from the mantle (*2*), and the core seems an improbable Xe reservoir (*3*), suggesting that the "missing" Xe must be trapped elsewhere. Ices (*4*), clathrates (*5*), and sediments (*6*) were first tested as potential Xe reservoirs, without success. Early escape from the atmosphere was suggested to explain the light-isotopic abundance pattern (*7*) of atmospheric Xe, but hydrodynamic escape models require that most of the primordial Xe be retained in the interiors of the planets (*8*). This Xe retention could be explained if the normally inert Xe became increasingly soluble or even formed compounds under the conditions found within planetary interiors, resulting in the depletion of Xe in the atmosphere. Experimentally, no reaction has been observed between Xe and Fe at pressures up to 70 GPa (*3*), and if Xe were denser than mantle materials (*9*), its extremely low concentration in the mantle leads us to question how gravitationally unstable particles are formed. The incompatible character of rare gases may vary with pressure ($P$) and temperature ($T$), and it


[1]Université Pierre et Marie Curie and Institut de Physique du Globe de Paris, 75252 Paris, France. [2]Bayerisches GeoInstitut, 95440 Bayreuth, Germany. [3]Laboratoire de Sciences de la Terre, Ecole Normale Supérieure de Lyon, 69364 Lyon, France. [4]School of Physics and Centre for Science at Extreme Conditions, University of Edinburgh, EH9 3JZ, UK. [5]European Synchrotron Radiation Facility, 38043 Grenoble, France.

*To whom correspondence should be addressed. E-mail: sanloup@ccr.jussieu.fr
†Present address: Geowissenschaftliches Zentrum, Goettingen University, 37077 Goettingen, Germany.